ORIGINAL RESEARCH ARTICLE

Phase Transformations in Third Generation Gamma Titanium Aluminides: Ti-45Al-(5, 10) Nb-0.2B-0.2C

NITISH BIBHANSHU, RASHI RAJANNA, AMIT BHATTACHARJEE, and SATYAM SUWAS

Third generation γ-titanium aluminides with nominal compositions Ti–45Al–5Nb–0.2B–0.2C and Ti–45Al–10Nb–0.2B–0.2C were investigated to identify the phase transformation and their morphological stability with temperature. Electron microscopy and differential scanning calorimetry were employed for the characterization of phases and for recording the corresponding transformations, respectively. It has been inferred that the order–disorder transformation temperatures $\alpha_2 \rightarrow \alpha$ increased with increasing Niobium (Nb), while the α-transus temperature decreases. The stability of the microstructure for both alloys with temperature were also investigated. Mass change measured for the heating rates 20 °C s^{-1} and 30 °C s^{-1} reveals that the alloy Ti–45Al–10Nb–0.2–0.2C shows stability up to 1100 °C, and the alloy Ti–45Al–5Nb–0.2B–0.2C is stable up to 900 °C. The orientation relationship between the phases indicates that with the change in shape of the α phase from lamellar to equiaxed, it deviates from the Blackburn orientation relationship.

I. INTRODUCTION

PROPERTIES of γ-titanium aluminides (TiAl: L1$_0$ crystal structure) such as oxidation resistance, high specific strength, good creep properties make these alloys good candidates for application in gas turbine engines.[1–3] However, low plasticity and poor fracture toughness are perceived to be the barrier for the application in the high-pressure turbine.[4,5] By reducing the Al content a second phase with the structure of stoichiometric Ti$_3$Al (α_2: DO$_{19}$ crystal structure) forms, which facilitates plasticity by twin formation during deformation at the interfaces of γ and α_2 phase.[6,7] The addition of a β-stabilizing element like Nb further enhances plasticity by stabilizing the softer, β or B2 phases. The ductility in the newer generation alloys has increased to 2.7 pct, which was attained by reducing aluminium and increasing the Nb content in the alloys.[8,9] At high temperature, these alloys possess additional plasticity due to the formation of twin boundaries by phase transformation.[10] Additionally,

the strength and plasticity of these alloys can be enhanced by getting modulated features in the microstructure.[11,12] The modulation in the microstructure was observed because of diffused boundary formation between the B2 and B19 structures.[11,12] The identification of such phase equilibria in these alloys has an impact in identifying the microstructural stability and further their applications. The role of alloying elements on phase transformation provides an idea of morphological phase stability which could trigger the mechanical properties' optimization.[13–15]

However, the quest for enhancing ductility and a further improvement in high-temperature properties of TiAl-based alloys require identification of their microstructural stability.[16,17] One of the methods of enhancing the morphological phase stability is by the change in the alloys' chemistry.[18–20] The ultimate success of these approaches will require a more detailed knowledge of high-temperature phase equilibria in complex Ti–A1–X alloys.[15,17,21] The current study examines the effects of Nb, a known β isomorphous stabilizing element, on phase stability in a 45 at. pct Al TiA1 alloys.[3,22,23] B is a known grain refiner[3,24,25] and a Carbon (C) addition increases transformation temperature, creep resistance and can also stabilize the α phase.[26,27] With increasing Nb content in the alloys, the β phase content in the melt increases during the solidification that leads to different microstructural features and morphologies at room temperature. It is known the α_2 and γ phase follows the Blackburn orientation relationship during the transformation,[28,29]

NITISH BIBHANSHU is with the Oak Ridge National Laboratory, Oak Ridge, TN 37831. Contact e-mail: nitishb@iisc.ac.in, nitishbibhanshu@gmail.com RASHI RAJANNA and SATYAM SUWAS are with the Department of Materials Engineering, Indian Institute of Science, Bangalore 560012, India. Contact e-mail: satyamsuwas@iisc.ac.in, satyamsuwas@gmail.com AMIT BHATTACHARJEE is with the Ti-alloy Group, Defence Metallurgical Research Laboratory, Hyderabad 500058, India.
Manuscript submitted February 26, 2021; accepted September 22, 2021.
Article published online October 9, 2021.

and the α and β obey a Burger's orientation relationship.[30,31]

Several studies have reported the effect of C and Nb on the phase transformation and oxidation resistance in γ-TiAl alloys.[3,12] But the literature is scarce on the effect of elements on the microstructural stability as a function of the temperatures. In the present study, phase transformation temperatures and microstructural stability for Ti–45Al–5Nb–0.2B–0.2C and Ti–45Al–10Nb–0.2B–0.2C alloys were examined using DSC, thermal gravimetric analysis (TGA), and microstructural investigation.

II. MATERIALS AND METHODOLOGY

A. Alloys and Sample Preparation

Five times vacuum arc melted, cast and hot isostatically pressed (HIPed) materials with the compositions Ti–45Al–5Nb–0.2B–0.2C and Ti–45Al–10Nb–0.2C–0.2B (hereafter, it will be referred to as Ti-45-5 and Ti-45-10, respectively) were received from Defence Metallurgical Research Laboratory, Hyderabad (India). The alloy pancakes were given a Deltaglaze FB 412® coating and HIPed at 1230 °C in an ASACO model No A650-09 hot isostatic press for four hours at a pressure of 120 MPa in an argon atmosphere.

For the identification of phase stability at different temperatures, small cubical blocks of dimension *3 mm X 3 mm X 3 mm* (weight ~ 70 mg) were extracted by electric discharge machining (EDM) from the pancakes. The location in the pancake from which of the samples extracted is shown in Figure 1. An extracted sample from the EDM was electropolished, followed by mechanical grinding. The electropolishing was performed at room temperature using LactroPol 5 (Struers) with A3 solution that has the composition of 60 mL perchloric acid, 600 mL methanol, and 360 mL butoxy ethanol. This electropolished sample was used for the microstructural investigations as well as for the X-ray diffraction experiment. The cast and HIPed alloys possess a lamellar microstructural feature.[7,32] The Ti-45-5 alloy had a strong lamellar orientation with respect to the solidification direction, whereas the Ti-45-10 alloy had a more random orientation of the lamellae and hence smaller colonies.[7,32]

B. Phase Stability and Heat Treatment

To determine the transformation temperatures in these alloys, samples were subjected to differential scanning calorimetry (DSC) and thermo-gravimetric analysis (TGA). The DSC was carried out in the temperature range of 1000 °C to 1450 °C, with a heating rate of 20 °C min⁻¹ in an argon atmosphere. The mass change was carried out for the samples with the same dimensions as used for phase transformation. Heating of the samples was carried out in atmospheric air and the change in mass was obtained for the temperature range 100 °C to 1450 °C at the two-heating rates, 20 and 30 °C min⁻¹. One heating rate we kept identical for the
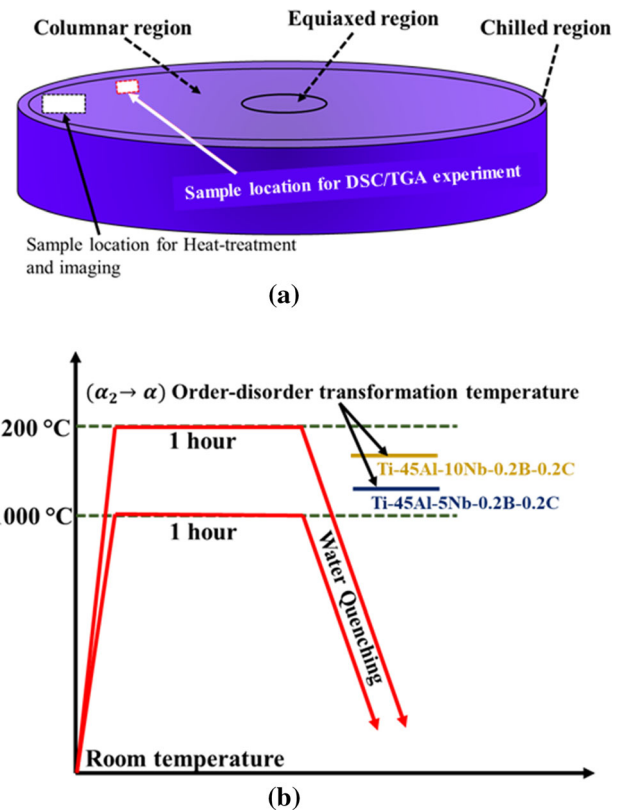

(a)

(b)

Fig. 1—Schematic of the (a) pancake depicting the chilled, columnar and equiaxed region and the locations of the samples extracted for DSC/TGA and the microstructural analysis. (b) Heat treatment cycle followed in the present study.

phase transformation and mass change; however, an additional heating rate of 30 °C min⁻¹ was to ensure the trend obtained for the mass change of the alloy.

The phase transformation temperatures for both alloys were determined by DSC and then detailed microstructural investigations were carried out on another set of samples. Both the alloys were subjected to identical conditions of the heat treatment for verification. Samples with the dimensions of *2 mm × 4 mm × 6 mm* and *Ø6 mm × 2 mm* for Ti-45-5 and Ti-45-10, respectively, were extracted from the pancakes (Figure 1). For high-temperature equilibrium microstructures, the samples were soaked at 1000 °C and 1200 °C for one hour and quenched into water. As air can influence the phases of the alloys, the heat treatments were done in air as well as vacuum. Heat treatments in vacuum were performed by sealing the sample in a quartz tube at a vacuum of 10⁻³ mbar. The sealed samples were also soaked for an hour at 1000 °C and 1200 °C. To freeze the high-temperature microstructure, samples were quenched into the water after the soaking. For the phase identification in the quenched samples, X-ray diffraction was carried out on the electropolished surface. For better resolution, X-ray diffractions patterns were recorded with a count time of 200 seconds for every 0.008 deg step in a PANalytical X'Pert diffractometer with CuK$_\alpha$ radiation.

C. Microstructural Characterization

Microstructural characterization was carried out using a scanning electron microscope (SEM, ESEM Quanta 200) and the images were captured in the backscattered electron (BSE) mode at 30 kV and a working distance of 8 mm. For examining the finer details of the microstructure, e.g. phase distribution, the orientation of grains, etc. the electron backscattered diffraction (EBSD) scan technique was employed. The EBSD scans were acquired on the FEI Helios Nano Lab™ Dual Beam™ (Thermo Fisher Scientific, Oregon) microscope and recorded data were analysed using TSL-OIM™ (EDAX) software. A few samples were also examined using transmission electron microscopy (TEM) in Technai T20 operated at 200 kV.

D. Mechanical Response

To understand the effect of microstructural variation on mechanical behaviour, Vickers microhardness measurements were carried out on the same plane on which microstructures (both BSE and EBSD) were recorded. The indentations were done using a load of 100 gf and a dwell time of 10 seconds. Ten measurements were performed for each condition. The distance between indents was 100 μm.

III. RESULTS

A. Initial Microstructures

The BSE micrographs of the cast and HIPed samples of Ti-45-5 and Ti-45-10 (initial condition) alloys are shown in Figure 2. The Ti-45-5 alloy exhibits lamellar features, with lamellae oriented at 45 deg with the solidification direction, whereas the Ti-45-10 alloy shows random orientation of the lamellae.

Figure 3 shows the microstructural features generated by EBSD scans, namely the phase maps superimposed on the image quality (IQ) maps, and the inverse pole figure (IPF) maps for the TiAl (γ) and Ti$_3$Al (α_2) phases. Using the phase maps, the content of α_2 phase was determined to be 4 pct in both the alloys. The dimensions of the β phase and its fraction were too small to be captured by the EBSD scan. The IPF map of the γ phase shows the two different types of orientation distribution of lamellae in the colonies. The distribution of α_2 phase is along the boundaries of the γ–γ lamellae as well as along the interfaces of γ grains (shown in Figures 2 and 3).

B. Identification of Phases at Different Temperatures

Differential scanning calorimetry (DSC) of both alloys is shown in Figure 4, which displays the exothermic heat evolution with temperature. In the titanium aluminide system, major transformations take place above 1000 °C, so the DSC data were plotted for the temperature range of 1000 °C to 1450 °C. The peaks in the curves correspond to a phase transformation. The range of the transformation temperatures are given in Table I and the peak transformation temperatures are given in Table II. The DSC curves indicate that while the $\alpha_2 \rightarrow \alpha$ transformation temperature increases by 55 °C when the Nb content increases from 5 to 10 pct, the α transus ($\gamma + \alpha \rightarrow \alpha$) temperature decreases by 25 °C (Grey ellipses in Figure 4). The transformation takes place over a range of temperatures (Table I). The DSC peak for the Ti-45-5 alloy indicates an $\alpha \rightarrow \alpha + \beta/\beta_2$ transformation at ~ 1412 °C; however, the Ti-45-10 alloy shows a small peak which corresponds to the $\alpha + \beta \rightarrow \beta$ transformation (Marked in the green shade).

These phases were also identified by X-ray diffraction patterns of the water-quenched samples (after 1 hr soaked at 1000 °C and 1200 °C) in air and vacuum. The samples heat-treated in air showed the peaks of both α_2 and γ phases at 1000 °C and 1200 °C in both the alloys (Figure 5). However, the Ti-45-10 alloy heat-treated in vacuum and quenched from 1200 °C showed the B2 phase (Figure 6) as well.
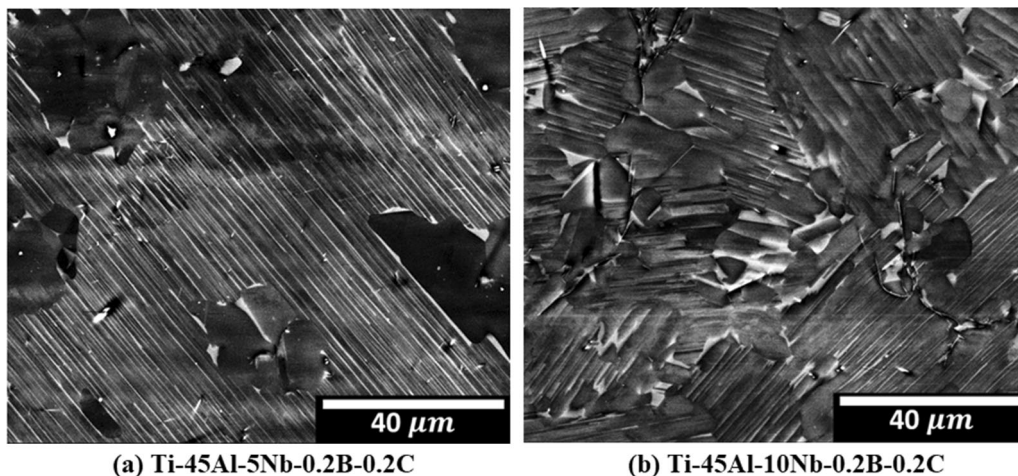

(a) Ti-45Al-5Nb-0.2B-0.2C   (b) Ti-45Al-10Nb-0.2B-0.2C

Fig. 2—Backscattered SEM micrographs of cast and HIPed (initial) condition of the alloys: (a) Ti–45Al–5Nb–0.2B–0.2C and (b) Ti–45Al–10Nb–0.2B–0.2C.
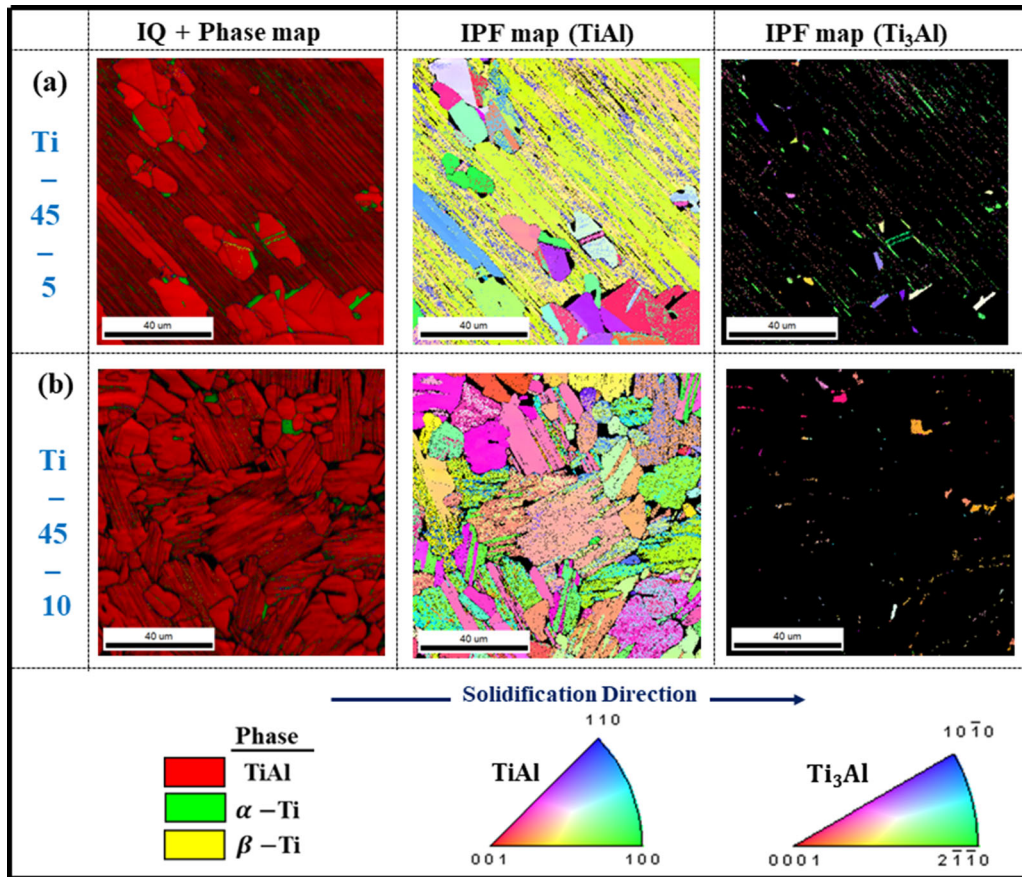
Fig. 3—Phase map superimposed on image quality map, the sample normal direction IPF map of the TiAl and Ti$_3$Al generated from EBSD of the initial condition for the alloys (*a*) Ti-45-5 and (*b*) Ti-45-10.
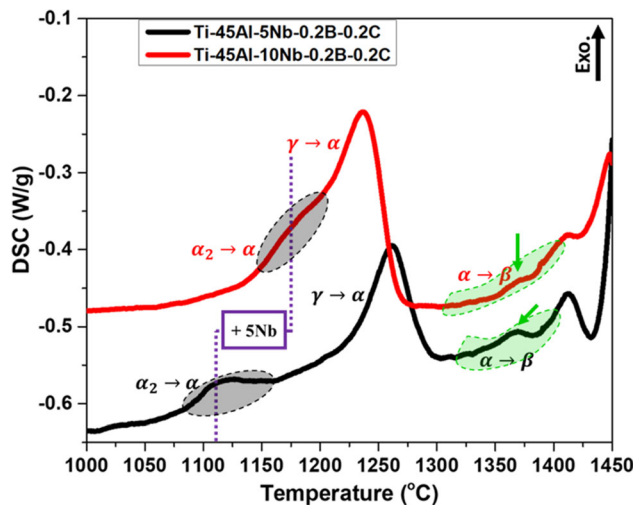

Fig. 4—DSC curves at the heating rate of 20 °C min^{-1} showing the exothermic heat evolution from phase transformation as a function of temperature for Ti–45Al–5Nb–0.2B–0.2C (black curve) and Ti–45Al–10Nb–0.2B–0.2C (red curve) (Color figure online).

C. *Effect of Temperature on Microtexture*

The (111)$_\gamma$ and (0001)$_{\alpha2}$ pole figures are plotted for both alloys covering more than 500 grains in the initial condition (Figure 7) and for the water-quenched samples from the temperature 1200 °C (Figure 8). The pole figures of the Ti-45-5 alloy display a very strong texture whereas the alloy Ti-45-10 shows a relatively weaker texture in the initial cast and HIPed condition. The (0001) pole figure of the α_2 phase shows maxima at similar location as the (111)$_\gamma$ pole figure of the γ phase. This indicates that the phases maintain the Blackburn orientation relationship in the cast and HIPed condition. For the α_2 phase, only one corresponding peak was observed for the Ti-45-5 alloy, whereas four corresponding peaks were observed in the Ti-45-10 alloy (Figure 7). For the samples heat-treated at 1200 °C, and water quenched (Figure 8), the heat-treated samples show maximum intensity at different orientations in the (111)$_\gamma$ pole figure compared to the pole figures of the cast and HIPed samples. This change in the peak intensity and orientations in the pole figure indicates a change in crystallographic orientation during heat

Table I. Range of Transformation Temperature for the Composition of Ti–45Al–5Al–0.2B–0.2C and Ti–45Al–10Nb–0.2C–0.2B

	Temperature (°C)		
Materials	$\alpha_2 \rightarrow \alpha$	$\gamma + \alpha \rightarrow \alpha$	$\alpha \rightarrow \alpha + \beta \rightarrow \beta/\beta + L$
Ti–45Al–5Nb–0.2B–0.2C	1090–1140	1140–1300	1348–1421
Ti–45Al–10Nb–0.2B–0.2C	1140–1195	1205–1270	1334–1430

Table II. Peak Transformation Temperature for the Composition of Ti–45Al–5Al–0.2B–0.2C and Ti–45Al–10Nb–0.2C–0.2B

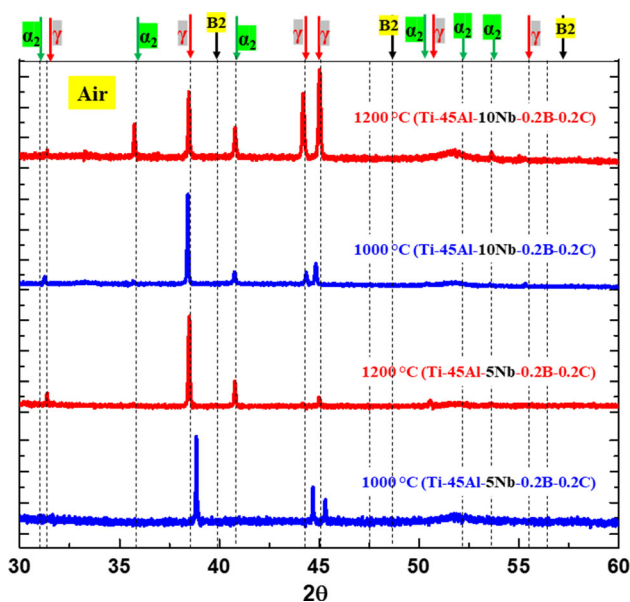|	Temperature (°C)		
Materials	$\alpha_2 \rightarrow \alpha$	$\gamma + \alpha \rightarrow \alpha$	$\alpha \rightarrow \alpha + \beta$	$\alpha \rightarrow \beta/\beta2 + \alpha$
Ti–45Al–5Nb–0.2B–0.2C	1115	1261	1368	1412
Ti–45Al–10Nb–0.2B–0.2C	1170	1236	1370	1400

Fig. 5—X-ray line profile of the water-quenched samples that were heat-treated at 1000 °C and 1200 °C, soaked for 1 hr in the air (temperature and composition for the Ti–45Al–5Nb–0.2B–0.2C and Ti–45Al–10Nb–0.2B–0.2C alloys are indicated in the figure near to the line profile).
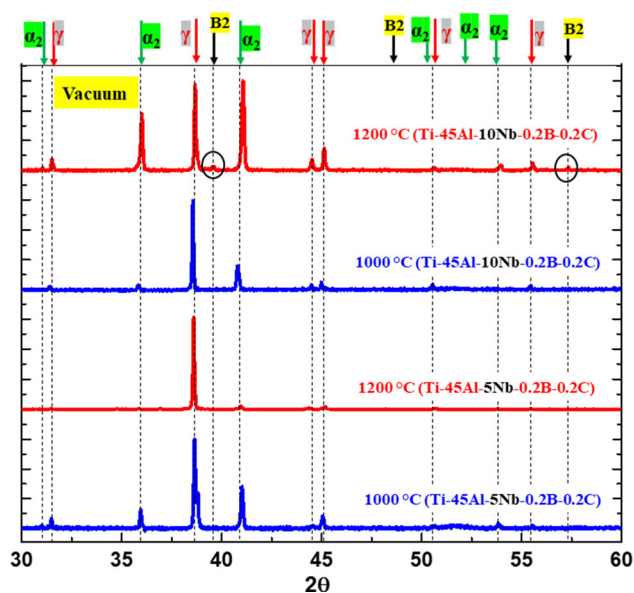

Fig. 6—X-ray line profile of the water-quenched samples that were heat-treated at 1000 °C and 1200 °C, soaked for 1 hr in vacuum/ quartz tube (temperature and composition for the Ti–45Al–5Nb–0.2B–0.2C and Ti–45Al–10Nb–0.2B–0.2C alloys are indicated in the figure near to the line profile).

treatment. However, the intensity maxima for both phases appear at nearly identical orientations in $(111)_\gamma$ and $(0001)_{\alpha2}$ pole figures (Figure 8) in both alloys, but for the Ti-45-10 alloy, some orientations show differences in relative intensity.

IV. ORIENTATION RELATIONSHIP AND MORPHOLOGY OF PHASES

The samples water quenched from 1200 °C show a number of microstructural features. The α_2 phase exhibits two types of morphologies in the microstructures of the Ti-45-5 alloy, needle-shaped and equiaxed.

On the other hand, the microstructure of the Ti-45-10 alloy displays mostly lamellar morphology for both the α_2 and γ phases. The IPF maps for the Ti-45-5 and Ti-45-10 alloys are shown in Figures 9(a) and (b), respectively.

To understand the orientation relationship between the two phases, the superimposed $(111)_\gamma$ and $(0001)_{\alpha2}$ pole figures are plotted. The grains are numbered from 1 to 7 for the Ti-45-5 alloy, and their orientation relationship is identified using arrows in pole figures 1 to 7. For the Ti-45-10 alloy, grains are numbered from 1 to 6, and pole figures representing the orientation relationships within individual grains are shown in Figure 9(b). A twinned γ-grain is shown in grain 5 for
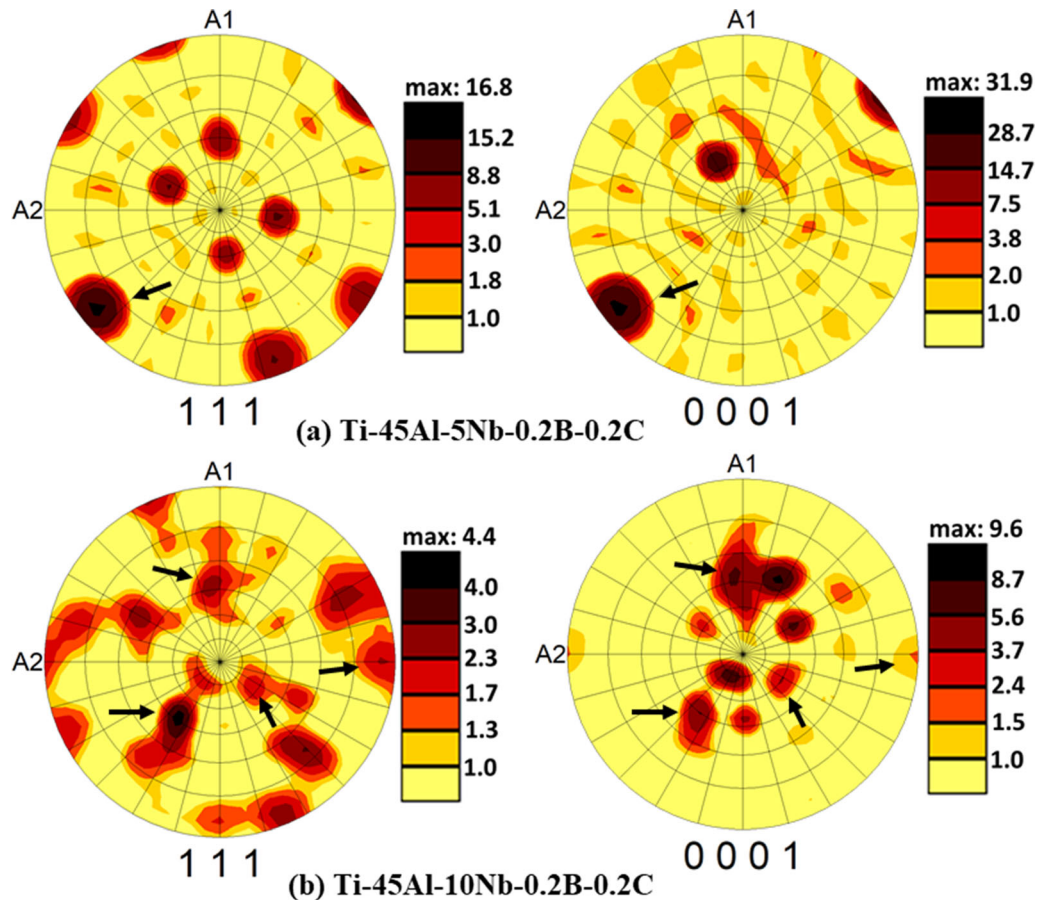
Fig. 7—The $(111)_\gamma$ and $(0001)_{\alpha2}$ pole figures for TiAl and Ti_3Al phases, respectively, for the cast and HIPed alloys (initial condition): (a) Ti–45Al–5Nb–0.2B–0.2C and (b) Ti–45Al–10Nb–0.2B–0.2C (marked black arrow represent the Blackburn orientation relationship).

the Ti-45-5 alloy which contains a needle-shaped α phase within the white twin (refer to grain 5 in Figure 9(a)). Along with these features, the microstructure also consists of equiaxed α grains. The microstructural features show that all the lamellar grains have the orientation relationship maintained with their parent grains, whereas the equiaxed α phase shows a deviation from the orientation relationship. The phenomena are identifiable from the superimposed pole figures generated for grains 1, 2, 4, and 5, and these grains are marked in Figure 9(a); however, similar instances are present in the Ti-45-10 alloy and presented by the pole figures of grain 1 and 2 of Figure 9(b). The higher fraction of the equiaxed α phase was observed for the water-quenched Ti-45-5 alloy. For the Ti-45-10 alloy, most of the grains show a strong orientation relationship maintained between the phases and exhibits lamellar microstructural features. Only at a few locations, equiaxed α grains were observed in the Ti-45-10 alloy which can cause a change from the Blackburn orientation relationship.

Additionally, titanium diboride (TiB_2) were observed in α colonies and γ (marked in grain 3 of Figure 9(a)), and their orientation is presented in the $(11\bar{2}1)_{TiB_2}$ pole figure that is superimposed with $(0001)_\alpha$ and $(111)_\gamma$ pole

figures of α and γ phase (pole figure of the grains 3 of Figure 9(a)).

A. Effect of Heat Treatment on Microhardness

Microhardness was measured for both the alloys in the initial condition as well as for the 1000 °C and 1200 °C heat-treated and water-quenched conditions. The hardness values were plotted as a function of heat treatment temperature in Figure 10. For both alloys, a similar trend is observed. The plot shows that the initial condition has higher hardness (410 HV for Ti-45-10 and 355 HV for Ti-45-5) than after heat treatment at 1000 °C /WQ (395 HV for Ti-45-10 and 310 HV for Ti-45-5). However, after heat treatment at 1200 °C/WQ, the hardness is higher, 435 HV for Ti-45-10 and 400 HV for Ti-45-5. The variation in microhardness depends on grain size, phase fraction, and phase morphology. These will be discussed in a subsequent section.

B. Effect of Heating Rate and Temperature on Mass Grain

The mass change was determined as a function of the temperature for two-heating rates of 20 and 30 °C min^{-1} (Figure 11). The plot shows that the mass
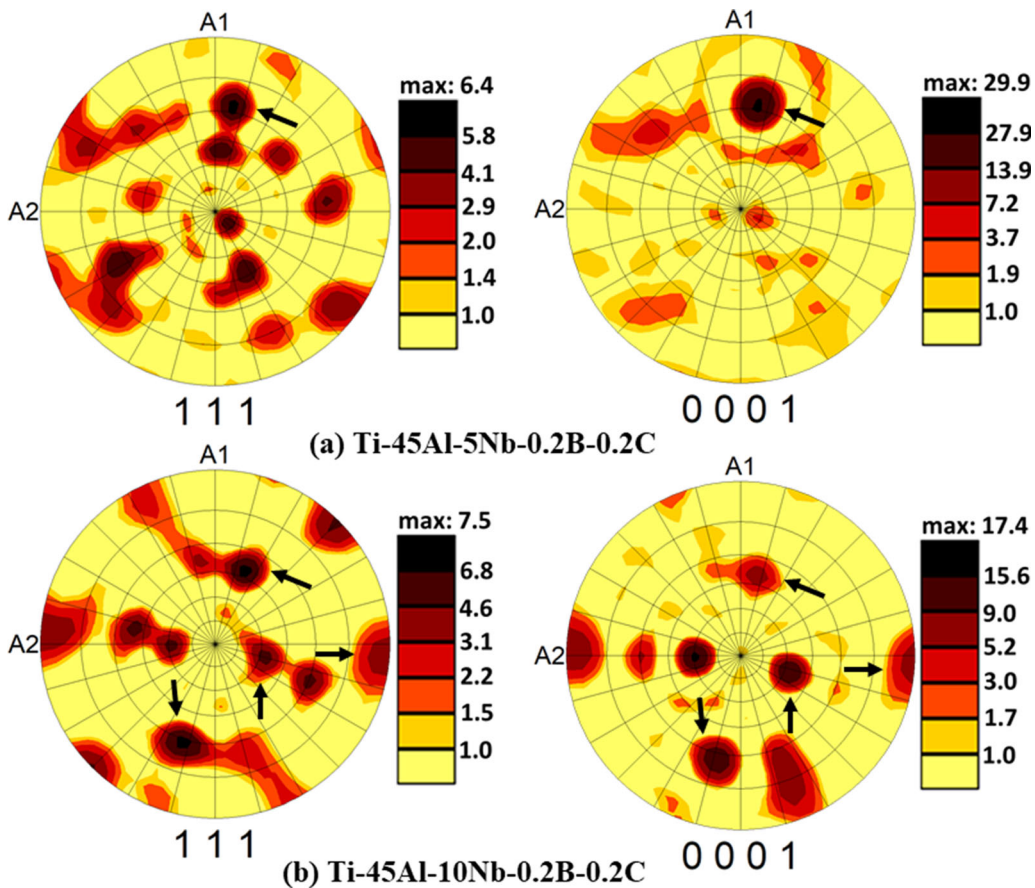
Fig. 8—The (111)$_\gamma$ and (0001)$_\alpha$ pole figures for TiAl and Ti$_3$Al phases, respectively, for the water-quenched samples from the temperature of 1200 °C and heat-treated in air, for the alloys: (a) Ti–45Al–5Nb–0.2B–0.2C and (b) Ti–45Al–10Nb–0.2B–0.2C (marked black arrow represent the Blackburn orientation relationship).

gain is negligible for Ti-45-5 and Ti-45-10 alloys upto ~ 900 °C and 1100 °C, respectively. For Ti-45-5, the mass gain appears to be faster for both the heating rates above 900 °C. On the other hand, the same trend is observed for Ti-45-10 alloy above 1100 °C. The plots indicate that the mass gain is higher for the Ti-45-5 below 1400 °C.

C. *TEM Investigation and Modulated Features*

The modulated microstructural features were recorded under the TEM for the water-quenched Ti-45-10 alloy from 1200 C that was heat-treated in air. The microstructure is shown in Figure 12. Along with modulated features, additional phenomena were also identified in this alloy that are associated with microstructural stability. Figure 12(a) shows a set of the parallel dislocations and this indicates that it belongs to the ordered structure. Also, at other locations, the modulation features observed in the α phase are shown in Figure 12(b) and a magnified image from a location within is presented in Figure 12(c) [note the scale bar]. Within this complex microstructure, annealing twins and stacking faults were also identified in the γ phase and they are marked by a yellow arrow and blue arrow, respectively, in Figures 12(d) and (f). Along with the formation of the modulated features in the α phase,

these features have also been observed near the interface of the α and γ phase as shown in Figure 12(e).

V. DISCUSSION

A. *Effect of Nb content*

Addition of Nb enlarges the β phase field in the binary Ti–Al phase diagram.[23,24] This is corroborated by the DSC curves (Figure 4). The curves also indicate that the ordering temperature for the transformation α → α$_2$ shifts towards the higher side by ~55 °C and the α (α + γ → α) transus temperature decreases by ~ 20 °C. A higher Nb content in the alloy Ti-45-10 causes an increase in the hardness also. Hardness depends on the microstructural features as well as microstructural constituents, which consists of the single phase γ, γ -γ lamellae as well as γ -α$_2$ lamellae.[22,33] The α$_2$/α phase has relatively higher strength then the γ phase.[34] Therefore, a higher fraction (number as well as area fraction) of the α phase in the colony can result in higher hardness.[35] The Ti-45-10 alloy has a higher α$_2$ phase fraction, which could account for the higher hardness of the Ti-45-10 alloy at the room temperature.

It is understood that the transformation temperature α$_2$ → α, as well as the temperature of single phase α field, depends on the Nb content. The results obtained from
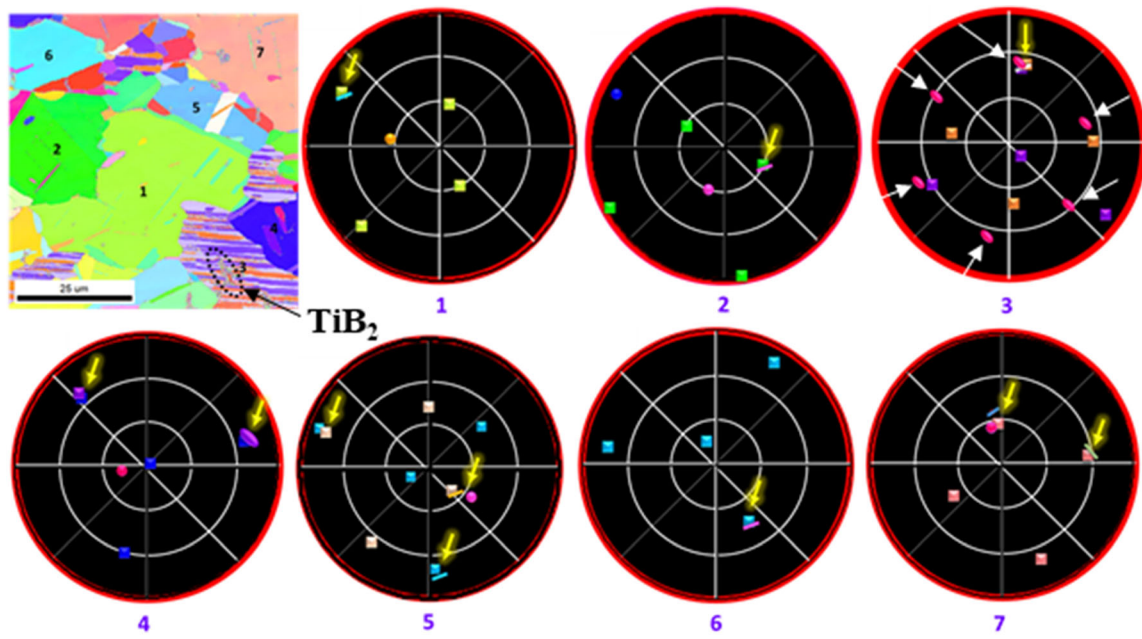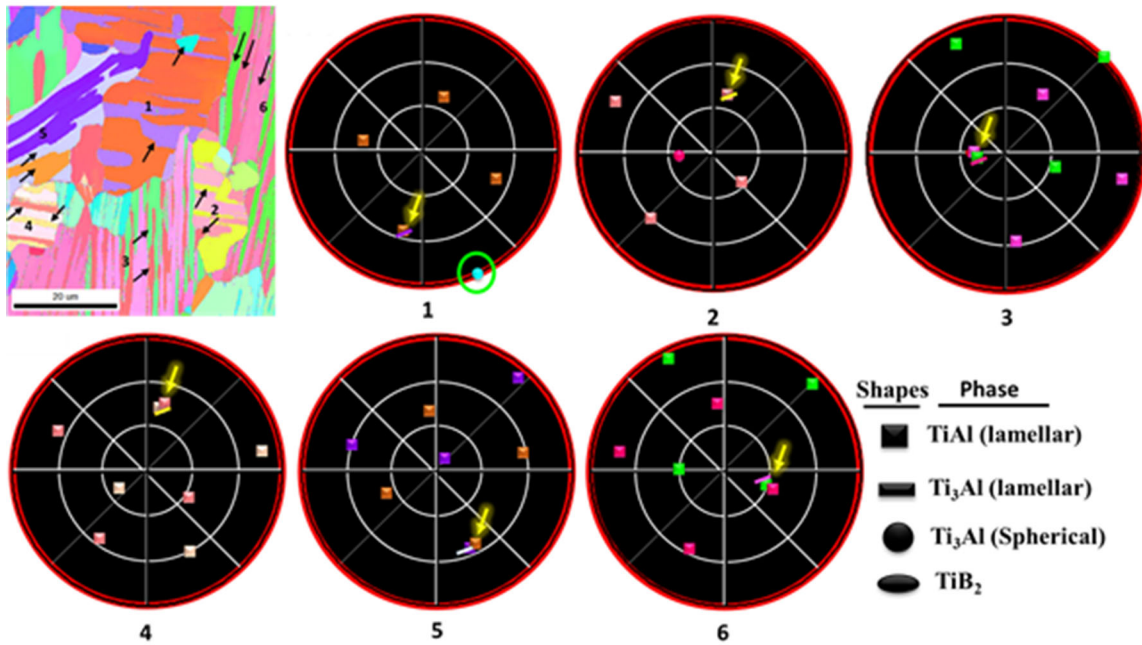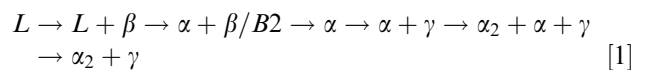
Fig. 9—Orientation relationship and orientation stabilization of the phases with respect to the parent grains (TiAl, Ti₃Al, and TiB₂) after heat treatment (1200 °C/1h/WQ) for the alloys (*a*) Ti–45Al–5Nb–0.2B–0.2C and (*b*) Ti–45Al–10Nb–0.2B–0.2C (In the pole figures, arrows indicate the planes exhibiting the orientation relationship, square shapes of the TiAl phase belongs to lamellae, rectangular shapes are of the Ti₃Al phase belongs to the lamellae, round shapes are from the globularized Ti₃Al and elliptical shape is from the TiB₂).

DSC indicates the range of $\alpha_2 \rightarrow \alpha$ phase transformation (Figure 4, Table I), for both the alloys. The range of transformation of the ordered phase (α_2) to the disordered phase (α) obtained in this study are 50 °C and 55 °C for the Ti-45-5 and Ti-45-10 alloys, respectively, and the temperature range for the transformation $\alpha + \gamma \rightarrow \alpha$ are 60 °C and 65 °C for the Ti-45-5 and Ti-45-10 alloy,

respectively. According to the phase diagram of Ti–45Al–xNb,[36] the solidification and transformation paths for the compositions Ti–45Al–5Nb and Ti–45Al–10Nb, respectively, are:

$$L \rightarrow L + \beta \rightarrow \alpha + \beta/B2 \rightarrow \alpha \rightarrow \alpha + \gamma \rightarrow \alpha_2 + \alpha + \gamma$$
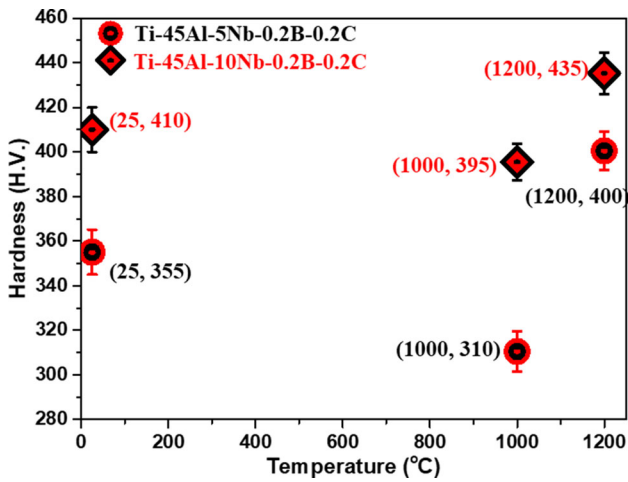$$\rightarrow \alpha_2 + \gamma \qquad [1]$$

Fig. 10—Microhardness for the cast and HIPed and water-quenched samples from the temperature of 1000 °C and 1200 °C. In the temperature profile, 25 °C is for the room temperature measurement.
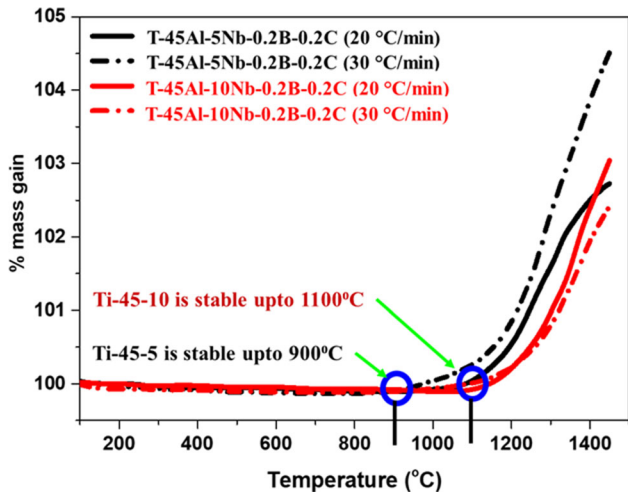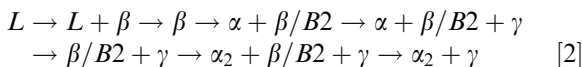

Fig. 11—TGA curve showing percent mass gain (100 pct is initial mass) as a function of temperature at the heating rate of 20 and 30 K/min for the alloys Ti–45Al–5Nb–0.2C–0.2C (black curve) and Ti–45Al–10Nb–0.2B–0.2C (red curve) (Color figure online).

$$L \rightarrow L + \beta \rightarrow \beta \rightarrow \alpha + \beta/B2 \rightarrow \alpha + \beta/B2 + \gamma$$
$$\rightarrow \beta/B2 + \gamma \rightarrow \alpha_2 + \beta/B2 + \gamma \rightarrow \alpha_2 + \gamma \quad [2]$$

However, it is worth mentioning that carbon (C) and boron (B) also influence the transformation temperatures which has been reported by several researchers.[17,36–38] Most of the C dissolves in the α/α_2 phase and stabilizes it, which enlarges the corresponding phase field in the phase diagram. The addition of the B causes the formation of borides which helps in grain to refine the microstructure by forming boride particles in the melt. With increasing β stabilizing elements, the TiB (stable at lower temperature) transforms to TiB$_2$ (stable at higher temperature).[3,39,40] The TiB and TiB$_2$ both were detected in EBSD scans of the water-quenched samples from the temperature of 1200 °C

(Figure 13). A higher fraction of TiB$_2$ is evident in Ti–45Al–10Nb–0.2B–0.2C (yellow arrow in Figure 14).

B. Shape of the α Phase and Orientation Relationship

The initial microstructures of both the alloys exhibit lamellar features. It is well known that grain coarsening takes place with higher heat treatment temperatures. However, in multi-phase alloys, the microstructure also undergoes a change of morphology and phase fractions depending on the phase field of the heat treatment. The alloy specimens that were heat-treated at 1000 °C/1 h/ WQ maintain their microstructural features with an increase in γ grain size for Ti-45-5 alloy and there is a relative increase in lamellar thickness for both alloys. However, the alloy specimens heat-treated at 1200 °C/ 1 h/WQ, show the presence of some equiaxed α phase within the γ grains and some along the grain boundaries in Ti-45-5 alloy. Needle-shaped α phase can also be identified in the parent γ grains. With the change of structure from lamellar to equiaxed, a deviation from the Blackburn orientation relationship occurred, which is possibly due to the decrease in coherency. The evidence is shown by the pole figures generated for individual grains (Figure 9) and in the phase map superimposed on an image quality map (Figure 13) and similar microstructural features can also be identified in the BSE micrograph (Figure 14). For the Ti-45-10 alloy, the α laths are thicker and equiaxed grains were also observed at some locations which were larger in size compared to the Ti-45-5 alloy.

The orientation relationship between phases of different morphologies (mainly α phase) was determined for both the alloys. To examine the orientation relationship, pole figures of closed packed $(111)_\gamma$ and $(0001)_{\alpha/\alpha_2}$ planes for the γ and α phases were superimposed. From the orientations of different γ grains, numbered from 1 to 7 and 1 to 6 for the alloys Ti-45-5 and Ti-45-10, respectively (Figure 9), it may be clearly concluded that the needle-shaped α phase maintains the orientation relationship of $(0001)_\alpha//(111)_\gamma$.[39,41–43] The deviation from the orientation relationship has been observed for α/α_2 phase grains that change shape from lamellar to globular. This indicates that the lamellar morphology of α and γ maintains their coherency; however, minimization of surface energy between these phases shows increasing incoherency, so the α phase changes its shape to globular. The deviation from the orientation relationship with the change of α phase shape to globular. This is most evident for the Ti-45-5 alloy in Figure 9(a) using the superimposed $(111)_\gamma$ and $(0001)_{\alpha/\alpha_2}$ pole figures of γ and α phase, respectively.

The Grain 5 of Ti-45-5 alloy (Figure 9(a)), shows a transformation twin that embodies a fine α phase at an angle about 45 deg to the twin boundary (Figure 9(a)). The α phase formed within the twin obeys the orientation relationship with the twin. The α phase evolved at the twin boundary grows towards the parent grains, maintaining the orientation relationship with the parent grains. However, the equiaxed grain of α phase evolved in Grain 5 shows incoherency with parent grains and
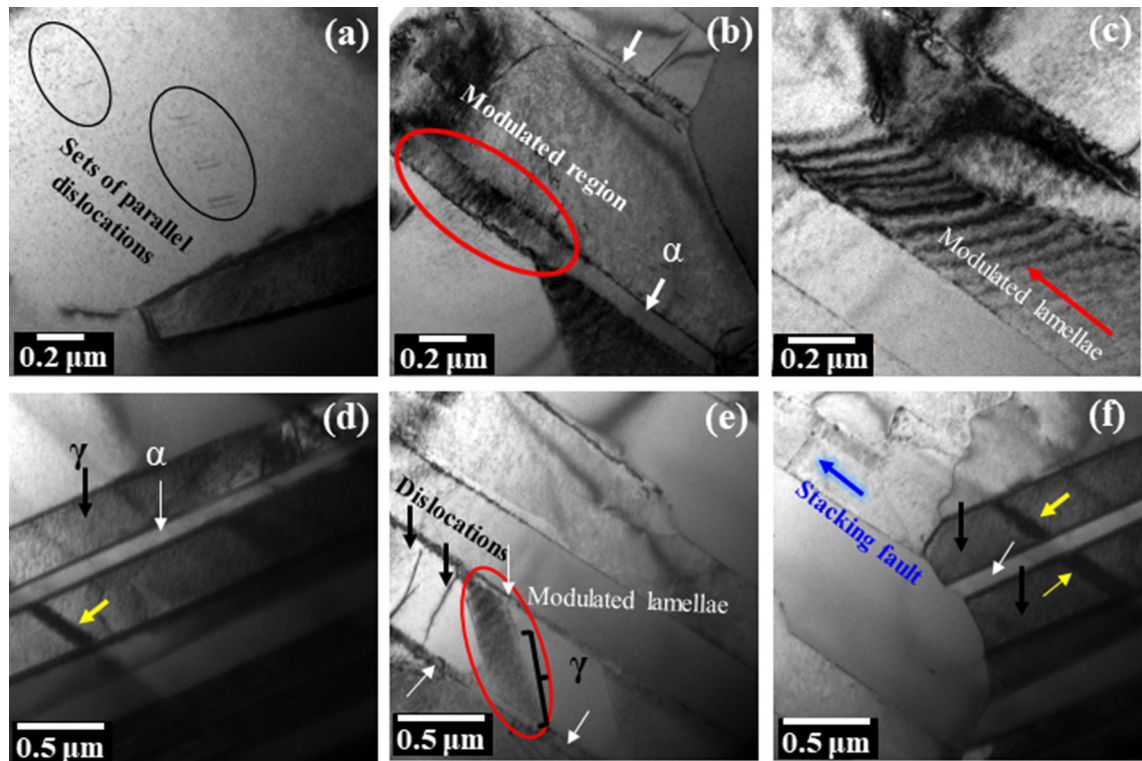
Fig. 12—TEM bright field images of Ti–45Al–10Nb–0.2B–0.2C samples after 1200°C/1h/WQ, showing (*a*) sets of parallel dislocations, (*b*) α phase with modulated lamellae in the intermediate region, (*c*) relatively higher magnifications of modulated lamellae, (*d*) lamellae of α and twinned γ phase, (*e*) formation of modulated lamellae at a certain angle in γ phase, and (*f*) stacking fault in γ phase.

about ~30 deg misoriented with respect to the parent grain orientation (refer to superimposed pole figures generated for Grain 5 in Figure 9(a)). On the other hand, the equiaxed grains distributed along the grain boundary maintain their coherency with their parent grain in both alloys.

Titanium diboride with stoichiometry TiB_2 is presented in Grain 3 in the Ti-45-5 alloy (Figure 9(a)). The orientation relationship of TiB_2 has also been investigated. It is well established that titanium boride (TiB) is a low-temperature stable phase, whereas titanium diboride (TiB_2) is a high-temperature stable phase.[25,39,44,45] In the lamellar grain, where all types of lamellae obey the orientation relationship, TiB_2 has been identified, and the orientation of the $(11\bar{2}\,1)$ plane of TiB_2 phase is parallel to the $(111)_\gamma$ and $(0002)_{\alpha2}$ plane of the γ and α_2 phase, respectively.

C. *Microstructural Stability and Microhardness*

The decrease in microhardness is greater for 1000 °C heat-treated and quenched Ti-45-5 sample alloy than in the Ti-45-10 sample (Figure 11). However, the hardness of the samples quenched after heat treatment at 1200 °C is higher than the cast and HIPed sample (initial condition). The increased hardness is correlated with the thickness of α laths and their fraction.[44,45] The microstructure shows the presence of two major phases in the samples water quenched after heat treatment at 1200 °C. The phase diagram of Ti-45Al-xNb reported in

the literature indicates that above 1140 °C, the alloy Ti-45Al-10Nb should possess only two phases β/B2 and γ phase.[46] In the present study the X-ray diffraction pattern of the Ti-45-10 sample quenched from 1200 °C, shows the presence of the B2 phase. However, for the quenched sample from 1000 °C, the B2 phase was not observed. On the other hand, quenched Ti-45-5 samples do not show any B2 peak. The diffraction patterns are consistent with the phase diagram reported for Ti-45Al-xNb. Carbon is an α phase stabilizer and along with some oxygen that invariably comes from metal powders, the α phase is stabilized at 1200 °C for the Ti-45-10 alloy, resulting in a slightly higher fraction of the α phase in the microstructures and that leads to the increased in the hardness value.

The evolution of mass with temperature for both alloys is shown in Figure 11. The higher Nb alloy shows better oxidation resistance, as the oxygen picked up (mass gain) for Ti-45-10 alloy is less at the heating rates of 20 and 30 °C/min. The higher rate of oxygen pickup for the Ti-45-5 alloy could be related to the lower amount of Nb in the alloy in comparison to Ti-45-10.

The oxidation resistance of γ-TiAl alloys can be enhanced by certain alloying additions which stabilize the Al_2O_3 phase and form oxides that are thermodynamically less stable than that of Al_2O_3. The objective is to add alloying elements which increase the activity of Al in the metal phases, decrease the concentration of oxygen-ion vacancies (V_O^{2-}) in TiO_2 and enhance Al diffusion in the metal phases; all of which promote the
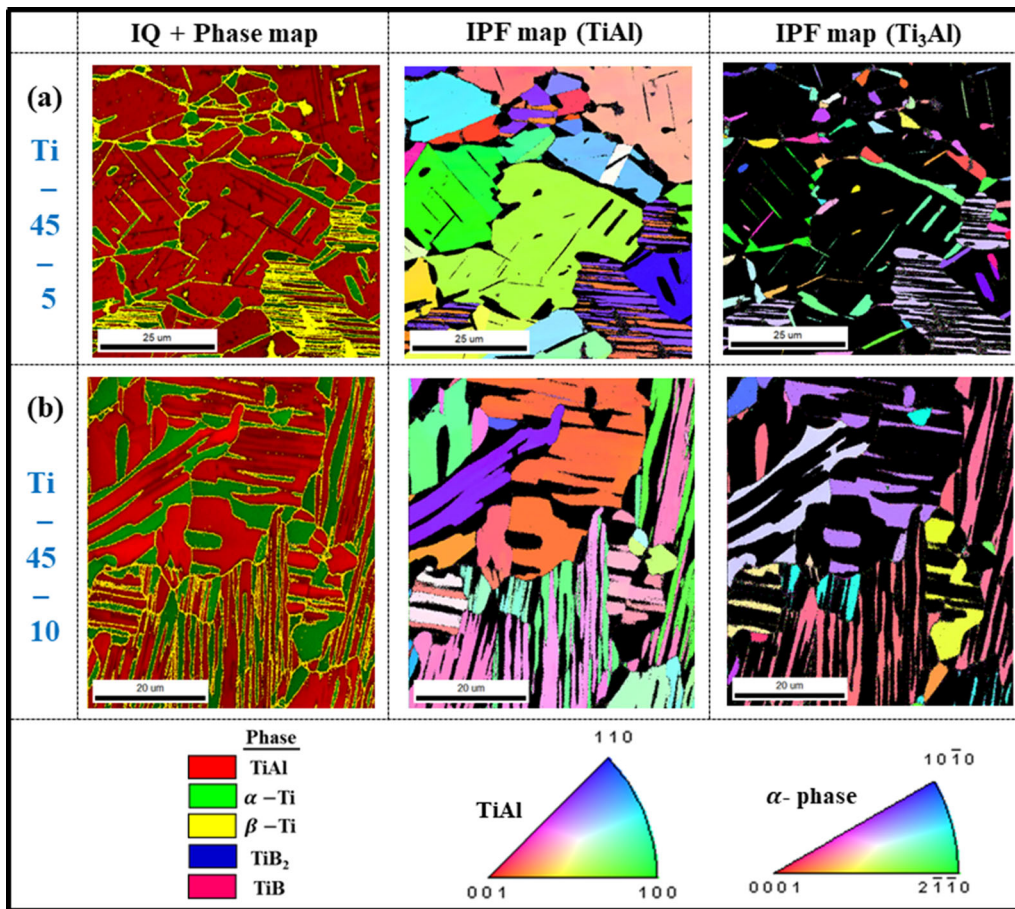
Fig. 13—Superimposed IQ and phase map and IPF maps of TiAl and Ti₃Al phases after heat treatment (1200 °C/1hr/WQ) for the (a) Ti-45-5 and (b) Ti-45-10 alloys, respectively.

formation of Al_2O_3 and moderate the formation of TiO_2.[41] Such beneficial effects can be achieved by minor additions of refractory elements, which have higher valence than Ti, *i.e.* W, Nb, Mo.[13–15,20,22,30,47] The higher valence refractory ions lower the growth rate of the TiO_2 by reducing the overall concentration of oxygen vacancies in the lattice, which thereby reduces the formation as well of diffusion of the Ti^{4+} ions.[15,28] The Ti-45-10 with higher Nb; therefore, shows a better oxidation resistance than Ti-45-5 is consistent with established understanding. As W, Nb, Mo, and Cr are β stabilizers, they also favour the formation of the β phase in these alloys. The higher diffusivity of Al in the β phase also promotes the outward diffusion of the Al atoms at the alloy/oxygen interface and enables the formation of the more protective Al_2O_3 phase in the oxide scale,[20,21] although the tendency to form β phase is lower in the alloy compositions of this study.

D. *Effect of Temperature on Microtexture*

Both alloys in the cast and HIPed condition obey the Burger's orientation relationship for α and β phase and the Blackburn orientation relationship for α and γ phases.[29,48] Whenever the phases lose their coherence, they show deviation from the orientation

relationship.[7,49] In the current study, globularization of the α/α_2 phase has been observed at some of the locations (Figure 9) and consequences of this phenomenon were to lose the coherency and result is a deviation from the orientation relationship. The intensity distribution in the $(0001)_\alpha$ pole figures has been observed at different locations in comparison to the $(111)_\gamma$ pole figures of Ti-45-5 alloy (Figures 8 and 9). However, for Ti-45-10, most of the intensity maxima has been observed at about similar locations in the $(111)_\gamma$ and $(0001)_\alpha$ pole figures. Deviation from the intensity maxima in the specified pole figures for these phases illustrates that several grains of the α phase change their shape under the influence of temperature. Understanding suggests that the crystallographic texture weakening under the influence of temperature is more dominant for the Ti-45-5 alloy.

E. *Modulated Microstructural Features*

Apple *et al.*[50] have reported the formation of the modulated lamellae. According to him, the alloys with nominal composition Ti–(40, 44)Al–8.5Nb that consists of a significant amount of the β phase stabilizers show modulated microstructural features under TEM. A
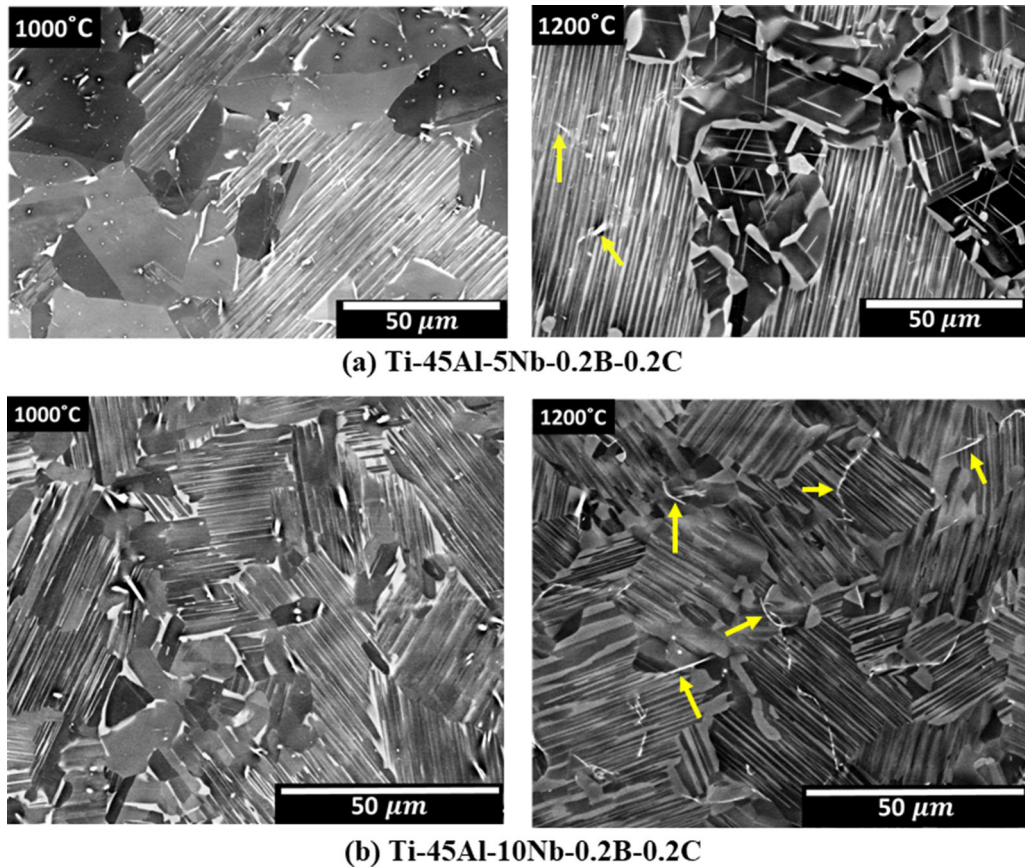
Fig. 14—Backscattered SEM micrographs after heat treatment (1200 °C/1h/WQ) for the (*a*) Ti-45-5 and (*b*) Ti-45-10 alloys, respectively (yellow arrows show that there is more TiB_2 in (*b*)) (Color figure online).

microstructure similar to pearlite has been reported by Tekeyama *et al.* for titanium aluminide.[51] Such features form by the $\alpha \rightarrow \beta$ (B2) + γ transformation, and in the domain of β (B2) phase, a modulated kind of microstructural features has been observed which consist of the alternate layers with a diffuse boundary between B2 (Pm3m) and B19 (Pmma) crystallographic structures.[52] For the present case, a TEM investigation on the 1200 °C water-quenched Ti-45-10 sample was carried out and modulated features were found within the α lath. The possible reason for the formation of modulated features in the α lath is because of the $\alpha \rightarrow \beta$(B2) + γ transformation. There is another possibility for the formation of the β phase by the supersaturation of the γ phase (supersaturation takes place by the β stabilizing elements, *e.g.* Nb). The supersaturated γ phase region, could act as a potent site for the formation of β phase, and hence the supersaturated regions lead to the formation of the modulated features in the Nb rich γ-TiAl alloys (Figures 12(b) and (c)). The movement of the partials (sets of dislocations is shown in Figure 12(a)) leads to the formation of the stacking fault (Figure 12(f)).

These faulted regions also possibly act as nucleation sites for the formation of modulated features. Another possibility of the transformation of the modulated lamellae to the γ structure has already been reported by Apple *et al.*[50] For the Ti-45-10 alloy, a connected γ

phase and modulated lamellar features are shown in Figure 12(e), which is possibly the intermediate stage for the formation of the γ phase from the modulated features or vice versa. Additionally, α_2 and γ lamellae are shown in Figure 12(d) consisting of annealing twins inside the γ phase (yellow arrows).

A lath with modulated features is divided into several regions with different crystalline structures.[50] These features sometimes exist without any sharp interfaces in between different crystallographic regions and the lattice mismatch between the modulated laths is accommodated by the interfacial dislocations and ledges.[11] According to Apple *et al.*, these modulated features, provide a unique combination of strength and ductility at room temperature as well as at high temperatures.[50]

VI. CONCLUSION

Third generation γ-Titanium aluminides of nominal compositions, Ti–45Al–5Nb–0.2B–0.2C and Ti–45Al–10Nb–0.2B–0.2C were investigated to understand their microstructural stability at different temperatures. Based on analysis of the experimental results, the following conclusion may be drawn:

1. In the higher Nb containing γ-TiAl alloys studied (Ti-45-10), the $\alpha_2 \rightarrow \alpha$ order–disorder

transformation temperature increases and the α transus temperature decreases.

2. The Ti-45-10 alloy is stable up to the temperature of 1100 °C and shows higher resistance to oxidation, whereas the alloy Ti-45-5 alloy shows resistance to oxidation only up to 900 °C.

3. The orientation stability of the α phase in the matrix of the γ phase depends on the morphology of the α phase. Equiaxed shaped α phase was observed to deviate by more the 15° from Blackburn's orientation relationship. The lamellar and needle type of α phase obey the orientation relationship with the matrix γ phase.

4. In the air, Ti-45-10 has higher microstructural stability as a function of the temperature and higher hardness compared to Ti-45-5 alloy.

5. In the Ti-45-5 alloy, the orientation of TiB_2 was determined in and around the lamellar colonies and observed that the $(11\bar{2}1)$ plane of TiB_2 was parallel to the (111) and (0002) planes of the γ and α phases, respectively.

6. A modulated microstructural feature has been observed in Ti-45-10 alloy, which is also one of the possible reasons for the high strength and ductility of these alloys.

REFERENCES

1. D. Daloz, U. Hecht, J. Zollinger, H. Combeau, A. Hazotte, and M. Založnik: *Intermetallics*, 2011, vol. 19, pp. 749–56.
2. Y. Wu, K. Hagihara, and Y. Umakoshi: *Intermetallics*, 2005, vol. 13, pp. 879–84.
3. U. Hecht, V. Witusiewicz, A. Drevermann, and J. Zollinger: *Intermetallics*, 2008, vol. 16, pp. 969–78.
4. R.J.E. Glenny, J.E. Northwood, and A.B. Smith: *Int. Mater. Rev.*, 1975, vol. 20, pp. 1–28.
5. P.B. Trivedi, E.G. Baburaj, A. Genã, L. Ovecoglu, S.N. Patankar, and F.H. Froes: *Metall. Mater. Trans. A*, 2002, vol. 33A, pp. 2729–34.
6. Y. Liang and J. Lin: *JOM*, 2017, 69.
7. N. Bibhanshu, A. Bhattacharjee, and S. Suwas: *J. Alloys Compd.*, 2020, vol. 832, p. 154584.
8. I. Agote, J. Coleto, M. Gutiérrez, A. Sargsyan, M. García de Cortazar, M.A. Lagos, I.P. Borovinskaya, A.E. Sytschev, V.L. Kvanin, N.T. Balikhina, S.G. Vadchenko, K. Lucas, A. Wisbey, and L. Pambaguian: *Intermetallics*, 2008, vol. 16, pp. 1310–16.
9. F. Klocke, D. Lung, M. Arft, P.C. Priarone, and L. Settineri: *Int. J. Adv. Manuf. Technol.*, 2013, vol. 65, pp. 155–63.
10. M.H. Yoo, C.L. Fu, and J.K. Lee: *J. Phys. III*, 1991, vol. 1, pp. 1065–84.
11. F. Appel, M. Oehring, and J.D.H. Paul: *Mater. Sci. Eng. A*, 2008, vol. 493, pp. 232–36.
12. M.W. Rackel, A. Stark, H. Gabrisch, N. Schell, A. Schreyer, and F. Pyczak: *Acta Mater.*, 2016, vol. 121, pp. 343–51.
13. S. Bolz, M. Oehring, J. Lindemann, F. Pyczak, J. Paul, A. Stark, T. Lippmann, S. Schrüfer, D. Roth-Fagaraseanu, A. Schreyer, and S. Weiß: *Intermetallics*, 2015, vol. 58, pp. 71–83.
14. N. Bibhanshu, G. Shankar, and S. Suwas: *J. Mater. Res.*, 2020, https://doi.org/10.1557/s43578-020-00079-0.
15. R.V. Ramanujan: *Int. Mater. Rev.*, 2000, vol. 45, pp. 217–40.
16. A. Couret, T. Voisin, M. Thomas, and J.P. Monchoux: *JOM*, 2017, vol. 69, pp. 2576–82.
17. M.N. Mathabathe, S. Govender, A.S. Bolokang, R.J. Mostert, and C.W. Siyasiya: *J. Alloys Compd.*, 2018, vol. 757, pp. 8–15.
18. D. Hu: *Intermetallics*, 2001, vol. 9, pp. 1037–43.
19. Z.G. Jiang, B. Chen, K. Liu, and Y.Y. Li: *Intermetallics*, 2007, vol. 15, pp. 738–43.
20. B. Liu, Y. Liu, C. Qiu, C. Zhou, J. Li, H. Li, and Y. He: *J. Alloys Compd.*, 2015, vol. 640, pp. 298–304.
21. O. Rios, S. Goyel, M.S. Kesler, D.M. Cupid, H.J. Seifert, and F. Ebrahimi: *Scr. Mater.*, 2009, vol. 60, pp. 156–59.
22. C.-J. Zhan, T.-H. Yu, and C.-H. Koo: *Mater. Trans.*, 2006, vol. 47, pp. 2588–94.
23. A. Gourgues, C. De Valduc, I. Tille, D. Ancizes, and L. Ancizes: 2016, pp. 209–14.
24. S. Roy, S. Suwas, S. Tamirisakandala, R. Srinivasan, and D.B. Miracle: *TMS 2009 - 138th Annu. Meet. Exhib. Febr. 15, 2009 - Febr. 19, 2009*, 2009, vol. 3, pp. 63–70.
25. D. Hu: *Intermetallics*, 2002, vol. 10, pp. 851–58.
26. H. Gabrisch, A. Stark, F.P. Schimansky, L. Wang, N. Schell, U. Lorenz, and F. Pyczak: *Intermetallics*, 2013, vol. 33, pp. 44–53.
27. M. Kastenhuber, B. Rashkova, H. Clemens, and S. Mayer: *Intermetallics*, 2015, vol. 63, pp. 19–26.
28. G. Dong Ren and J. Sun: *Acta Mater.*, 2018, 144.
29. S.R. Dey, E. Bouzy, and A. Hazotte: *Intermetallics*, 2006, vol. 14, pp. 444–49.
30. S. Suwas and R.K. Ray: *Bull. Mater. Sci.*, 1999, vol. 22, pp. 581–84.
31. R.K. Ray and S. Suwas: *Met. Mater. Int.*, 2000, vol. 6, pp. 39–49.
32. N. Bibhanshu, A. Bhattacharjee, and S. Suwas: *JOM*, 2019, pp. 1–13.
33. H. Ding, G. Nie, R. Chen, J. Guo, and H. Fu: *Mater. Des.*, 2012, vol. 41, pp. 108–13.
34. F. Kong, Y. Chen, and F. Yang: *Intermetallics*, 2011, vol. 19, pp. 212–16.
35. S.L. Semiatin, V. Seetharaman, and V.K. Jain: *Metall. Mater. Trans. A*, 1994, vol. 25A, pp. 2753–68.
36. E. Gamsjäger, Y. Liu, M. Rester, P. Puschnig, C. Draxl, H. Clemens, G. Dehm, and F.D. Fischer: *Intermetallics*, 2013, vol. 38, pp. 126–38.
37. S.L. Semiatin, V. Seetharaman, D.M. Dimiduk, and K.H.G. Ashbee: *Metall. Mater. Trans. A*, 1998, vol. 92A, pp. 7–18.
38. H.F. Chladil, H. Clemens, H. Leitner, A. Bartels, R. Gerling, F.P. Schimansky, and S. Kremmer: *Intermetallics*, 2006, vol. 14, pp. 1194–98.
39. D. Hu, C. Yang, A. Huang, M. Dixon, and U. Hecht: *Intermetallics*, 2012, vol. 23, pp. 49–56.
40. D. Hu: *Rare Met.*, 2016, vol. 35, pp. 1–14, https://doi.org/10.1007/s12598-015-0615-1.
41. D. Hu and H. Jiang: *Intermetallics*, 2015, vol. 56, pp. 87–95.
42. N. Bibhanshu and S. Suwas: *Mater. Sci. Forum*, 2018, vol. 941, pp. 1391–96.
43. G. Nolze, V. Geist, R. Saliwan-Neumann, and M. Buchheim: *Cryst. Res. Technol.*, 2005, vol. 40, pp. 791–804.
44. A.V. Kartavykh, M.V. Gorshenkov, V.V. Tcherdyntsev, and D.A. Podgorny: *J. Alloys Compd.*, 2014, vol. 586, pp. 153–58.
45. M. Oehring, A. Stark, J.D.H. Paul, T. Lippmann, and F. Pyczak: *Intermetallics*, 2013, vol. 32, pp. 12–20.

46. H.F. Chladil, H. Clemens, G.A. Zickler, M. Takeyama, E. Kozeschnik, A. Bartels, T. Buslaps, R. Gerling, S. Kremmer, L. Yeoh, and K.D. Liss: *Int. J. Mater. Res.*, 2007, vol. 98, pp. 1131–37.
47. O.P. Modi, N. Deshmukh, D.P. Mondal, A.K. Jha, A.H. Yegneswaran, and H.K. Khaira: *Mater. Charact.*, 2001, vol. 46, pp. 347–52.
48. R. Shi, H.L. Fraser, and Y.N. Wang: *Acta Mater.*, 2014, vol. 75, pp. 156–66.
49. S.R. Dey, A. Morawiec, E. Bouzy, A. Hazotte, and J.J. Fundenberger: *Mater Lett*, 2006, vol. 60, pp. 646–50.
50. F. Appel, J.D.H. Paul, M. Oehring: *Gamma Titanium Aluminide Alloys*, First, Wiley-VCH Verlag GmbH & Co. KGaA, Germany, 2011.
51. M. Takeyama and S. Kobayashi: *Intermetallics*, 2005, vol. 13, pp. 993–99.
52. F. Appel, M. Oehring, and J. Paul: *Mater. Res. Soc. Symp. Proc.*, 2007, vol. 980, pp. 383–88.